Supplementary Material for:
Single-Shot Narrowband Link Discovery via Space-Polarization Encoded Metasurfaces

Haoze Chen and Yasaman Ghasempour

Department of Electrical and Computer Engineering, Princeton University,
41 Olden St, Princeton, NJ 08544, USA.

Contents

Supplementary Note 1: Noise Modeling and Feature-Space Distance

In the main manuscript, polarization signatures are first compared using a balanced Euclidean distance in the two-dimensional feature space $\{\rho, \Delta\phi\}$. This distance is useful for visualizing the signature constellation and describing separability under a uniform feature-space noise assumption. However, when computing the probability of confusing one polarization signature with another, the effective distance should also depend on the observation uncertainty around the true angle, which is different across the field of view (FoV) since the noise variance of ρ and $\Delta\phi$ varies with local magnitudes of H- and V-polarized electric fields. Here, we derive a practical angle-dependent feature-noise model, which leads to a Mahalanobis generalization of distance computation used in forming our optimization objective.

Towards a given angle θ_k, we denote the intended H- and V-polarized electric fields as $E_H = A_H e^{j\phi_H}$ and $E_V = A_V e^{j\phi_V}$, where A_H, A_V are field amplitudes and ϕ_H, ϕ_V are phases. Under measurement noise, the observed fields can be modeled as $\tilde{E}_H = E_H + n_H$ and $\tilde{E}_V = E_V + n_V$, where n_H and n_V are noise independently sampled from the same circularly-symmetric complex normal distribution $\mathcal{CN}(0, \sigma^2)$. We assume that the optimized radiation pattern avoids deep nulls in both polarization channels, such that the noise level is significantly below the signal magnitudes across the FoV. For derivation purposes, we represent n_H, n_V in rectangular forms as $a + jb$, where $a, b \sim \mathcal{N}(0, \sigma^2/2)$.

We start by deriving the phase and magnitude noise in $\tilde{E}_H$. Without loss of generality, we rotate the electric field such that the intended field lies along the real axis (i.e., $E_H = A_H$). Under measurement noise, the observed field becomes $\tilde{E}_H = A_H + a + jb$. Subsequently, the phase noise can be calculated as:

$$\delta\phi_H = \arctan\left(\frac{b}{A_H + a}\right). \tag{S1}$$

Under small angle approximation, and since $a, b \ll A_H$, Eq.(S1) can be approximated with:

$$\delta\phi_H \approx \frac{b}{A_H + a} \approx \frac{b}{A_H}. \tag{S2}$$

From Eq.(S2), the phase noise in $\tilde{E}_H$ follows a Gaussian distribution with variance $\frac{\sigma^2}{2A_H^2}$. Similarly, the phase noise in $\tilde{E}_V$ follows a Gaussian distribution with variance $\frac{\sigma^2}{2A_V^2}$.

Regarding magnitude noise, the measured magnitude can be written as:

$$\tilde{A}_H = \sqrt{(A_H + a)^2 + b^2} = (A_H + a)\sqrt{1 + \frac{b^2}{(A_H + a)^2}}. \tag{S3}$$

Since $\frac{b^2}{(A_H+a)^2} \ll 1$, Eq.(S3) can be approximated with:

$$\tilde{A}_H \approx A_H + a. \tag{S4}$$

Under dB scale and first-order Taylor expansion around A_H, Eq.(S4) can be further derived into the following:

$$20\log_{10}\tilde{A}_H \approx 20\log_{10}(A_H + a) \approx 20\log_{10} A_H + \frac{20}{\ln 10}\cdot\frac{a}{A_H}. \tag{S5}$$

Hence, the magnitude noise of $\tilde{E}_H$ in dB scale can be written as:

$$\delta A_H[\mathrm{dB}] \approx \frac{20}{\ln 10}\cdot\frac{a}{A_H}. \tag{S6}$$

From Eq.(S6), the magnitude noise also follows a Gaussian distribution with variance $\left(\frac{20}{\ln 10}\right)^2 \cdot \frac{\sigma^2}{2A_H^2}$. Similarly, the magnitude noise in $\tilde{E}_V$ follows a distribution with variance $\left(\frac{20}{\ln 10}\right)^2 \cdot \frac{\sigma^2}{2A_V^2}$.

Following Eq.(S2) and Eq.(S6), the feature space noise can be derived as:

$$\begin{cases} \delta\rho = \delta A_V[\mathrm{dB}] - \delta A_H[\mathrm{dB}] \approx \dfrac{20}{\ln 10}\left(\dfrac{a_V}{A_V} - \dfrac{a_H}{A_H}\right) \\ \delta\Delta\phi = \delta\phi_V - \delta\phi_H \approx \dfrac{b_V}{A_V} - \dfrac{b_H}{A_H} \end{cases} \tag{S7}$$

As such, noise in both feature dimensions ρ and $\Delta\phi$ can be approximated with zero-mean Gaussian random variables, with the following angle-dependent variances:

$$\begin{cases} \sigma_{\rho,k}^2 \approx \left(\dfrac{20}{\ln 10}\right)^2 \left(\dfrac{\sigma^2}{2A_{V,k}^2} + \dfrac{\sigma^2}{2A_{H,k}^2}\right) \\ \sigma_{\Delta\phi,k}^2 \approx \dfrac{\sigma^2}{2A_{V,k}^2} + \dfrac{\sigma^2}{2A_{H,k}^2} \end{cases} \tag{S8}$$

Based on the derived variances, the feature-space noise around the true angle θ_k can be modeled with a covariance matrix $\mathbf{\Sigma}_k$ as:

$$\begin{bmatrix} \delta\rho_k \\ \delta\Delta\phi_k \end{bmatrix} \sim \mathcal{N}\left(\begin{bmatrix} 0 \\ 0 \end{bmatrix}, \mathbf{\Sigma}_k\right), \text{where } \mathbf{\Sigma}_k = \begin{bmatrix} \sigma_{\rho,k}^2 & 0 \\ 0 & \sigma_{\Delta\phi,k}^2 \end{bmatrix}. \tag{S9}$$

We note that the off-diagonal terms of $\mathbf{\Sigma}_k$ are zero because the noise in ρ and $\Delta\phi$ are uncorrelated. This is explicitly shown in Eq. (S7), where the in-phase (a) and quadrature (b) components are independent under circularly-symmetric complex Gaussian noise.

Given two polarization signatures at angles θ_k and θ_j, we define their feature-space difference as $\Delta\mathbf{s}_{kj} = [\rho_k - \rho_j,\ \mathrm{wrap}(\Delta\phi_k - \Delta\phi_j)]^\mathsf{T}$. The squared Mahalanobis distance from the true signature at θ_k to the candidate signature at θ_j can then be calculated as:

$$d_{kj}^2 = \Delta\mathbf{s}_{kj}^\mathsf{T} \boldsymbol{\Sigma}_k^{-1} \Delta\mathbf{s}_{kj}. \tag{S10}$$

With a diagonal covariance matrix, Eq.(S10) can be written explicitly as:

$$d_{kj}^2 = \frac{(\rho_k - \rho_j)^2}{\sigma_{\rho,k}^2} + \frac{[\mathrm{wrap}(\Delta\phi_k - \Delta\phi_j)]^2}{\sigma_{\Delta\phi,k}^2}. \tag{S11}$$

This distance generalizes the balanced Euclidean distance used for visualization in the main manuscript. Intuitively, two signatures with the same geometric separation in the $\{\rho, \Delta\phi\}$ feature space can have different effective separations depending on the local measurement uncertainty. If either polarization channel is weak at the true angle θ_k, the variances $\sigma_{\rho,k}^2$ and $\sigma_{\Delta\phi,k}^2$ increase as derived in Eq.(S8), reducing the effective separation and making the corresponding signature more susceptible to noise-induced confusion. Conversely, signatures observed with stronger polarization components have smaller feature-space uncertainty and therefore larger effective separation under the Mahalanobis distance. Finally, we use this angle-dependent distance to form the confusion probability in the metasurface optimization objective, as shown in the main manuscript.

Supplementary Note 2: C-Shaped Split-Ring Resonators

Here, we provide an electromagnetic primer on the C-shaped split-ring resonators (SRRs) used to realize the anisotropic array response required for single-shot, narrowband link discovery. In particular, we explain how the geometry of a C-shaped SRR gives rise to polarization-dependent resonances, and how arranging such resonators across an aperture can impose phase gradients for radiation pattern control.

As explained in the main manuscript and also shown here in Fig. S1a, the geometry of a C-shaped SRR is characterized by several parameters, including the outer radius r_{out}, the strip width w, the split opening angle β, and the in-plane orientation of the resonator α. The anisotropic response of this structure can be modeled by decomposing the incident electric field onto two orthogonal axes: the symmetry axis u and the gap axis v. When the incident electric field is polarized along u, surface currents are primarily induced along the two arms of the resonator, leading to a *plasmon resonance*. In contrast, when the incident electric field is polarized along v, the gap capacitance and the metallic loop inductance form *LC resonances*, producing a distinct frequency response. As such, the same physical resonator exhibits different complex transmission coefficients t_u and t_v depending on the incident polarization.

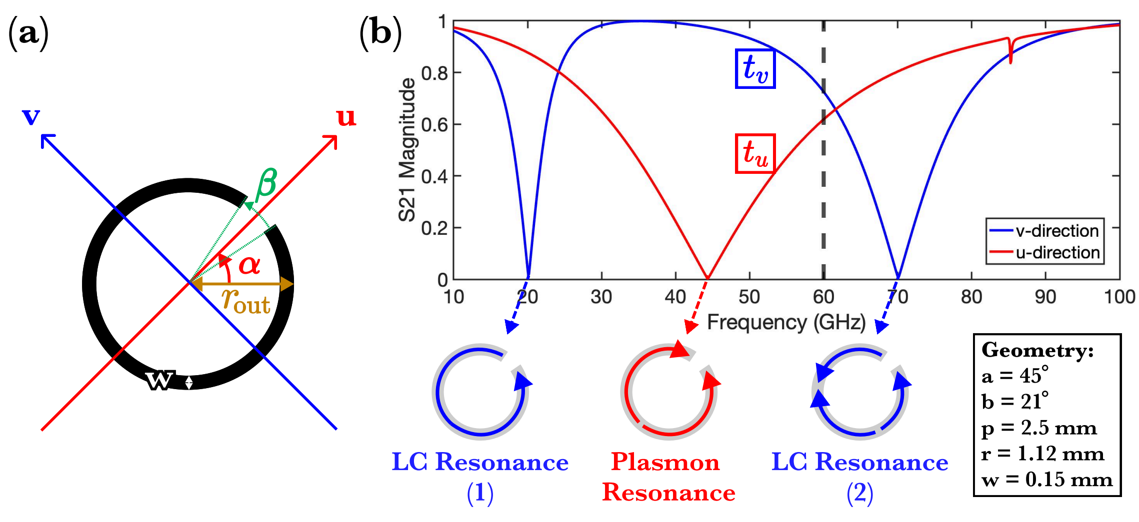

Figure S1: (a) Geometric characterization of a C-shaped split-ring resonator (SRR). (b) The two fundamental resonance modes of an example SRR.

Fig. S1b shows the full-wave simulation results of an example millimeter-scale meta-element, including the transmission magnitude coefficients along both principal axes. The resonant dips indicate frequencies at which the incident wave strongly couples to the corresponding resonance mode, reducing transmission through the cell. Since the resonance frequencies are controlled by the C-shaped geometry, changing r_{out}, w, and β modifies both the amplitude and phase of t_u and t_v at a specific evaluated frequency (e.g., 60 GHz in this example). For an arbitrary incident polarization, both modes are excited simultaneously according to the field projection onto u and v. The transmitted field is then formed by recombining these two components after they experience different transmission coefficients. This anisotropic recombination is the physical mechanism that enables polarization conversion.

In addition, the same anisotropic response can be used for radiation pattern control when many SRRs are arranged into a metasurface aperture. As in conventional array theory, diverse radiation patterns can be shaped with carefully-designed phase profiles. For C-shaped SRRs, a wide phase control range can be realized in the cross-polarized channel (e.g., V-polarized incidence and H-polarized transmission) by changing the resonator geometry. As a simple example, Fig. S2a shows four C-shaped SRRs selected to provide approximately 90° phase increments in the cross-polarized transmission coefficient, while keeping transmission magnitudes identical. When these elements are periodically arranged to form a gradient, the cross-polarized radiation is steered toward an off-broadside direction, as shown in Fig. S2b.

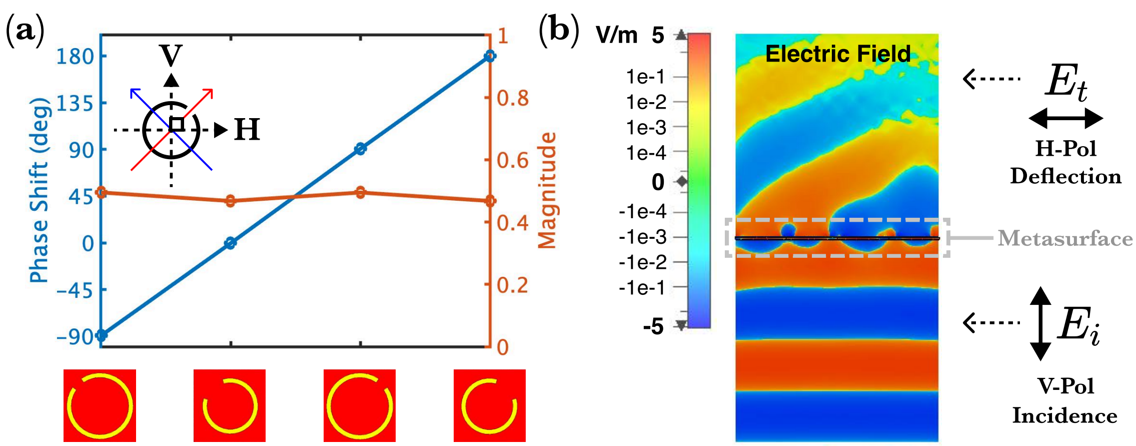

Figure S2: (a) Cross-polarization transmission coefficients of a set of designed meta-elements. (b) Simulated deflection under array arrangement.

Overall, C-shaped SRRs provide a compact and passive mechanism for coupling polarization conversion with wavefront shaping. This operating principle lays the foundation for the metasurface model used in the main manuscript, where each element contributes anisotropic transmission responses to form the polarization-resolved radiation patterns $F_H(\theta)$ and $F_V(\theta)$.

Supplementary Note 3: Unit-Cell Dictionary and Optimization Space

We numerically model metasurfaces as discrete arrays of SRR meta-elements, where each unit cell contributes coupled co- and cross-polarized transmission responses. In practice, these responses cannot be chosen arbitrarily because they are jointly determined by the physical geometry of each resonator, as discussed in Supplementary Note 2. Thus, to limit the optimization space to physically realizable radiation patterns, we construct a full-wave-derived dictionary of obtainable unit-cell responses and optimize the metasurface layout over this discrete design space.

To construct such a dictionary, we sweep three geometric parameters: the outer radius r_{out}, the split opening angle β, and the metallic strip width w. Full-wave simulations are conducted in CST Studio Suite with unit-cell boundary conditions at 140 GHz. The sweep ranges are $r_{\text{out}} = 0.4$–0.5 mm with a step size of 0.01 mm, $\beta = 1°$–$179°$ with a step size of $1°$, and $w = 0.15$–0.30 mm with a step size of 0.05 mm. This produces $11 \times 179 \times 4 = 7876$ simulated C-shaped SRR geometries.

For every simulated geometry, we extract the complex transmission coefficients corresponding to the co-polarized and cross-polarized responses. Fig. S3 visualizes the resulting dictionary across r_{out} and β for different values of w. For C-shaped SRRs, the co-polarized response generally maintains a higher transmission magnitude, which corresponds to the portion of the incident field that passes through the surface without strong polarization conversion. However, its accessible phase range is more limited, making it less effective for arbitrary radiation pattern synthesis on its own, which often leaves a strong broadside beam component. In contrast, the cross-polarized response generally exhibits lower transmission magnitude under a polarization-conversion loss, but provides a much wider phase-control range, achieving full 2π coverage over the simulated geometries (after rotation). This cross-polarized phase diversity is important for shaping angle-dependent polarization signatures. These trends highlight that the metasurface design space is non-trivial: The co- and cross-polarized responses are physically coupled through the same SRR geometry, and their amplitude/phase tradeoffs are asymmetric. Therefore, the metasurface must be optimized over the joint dictionary of physically realizable responses.

As described in the main manuscript, we further include the 90°-rotated version of each simulated unit cell, which doubles the design space from 7876 to 15752 candidate states.

This formulation ensures that full polarization control can be achieved. As such, every candidate layout corresponds to a metasurface that can be fabricated from known C-shaped SRR geometries. The resulting search space is discrete, high-dimensional, and strongly coupled across elements, motivating the use of a genetic algorithm.

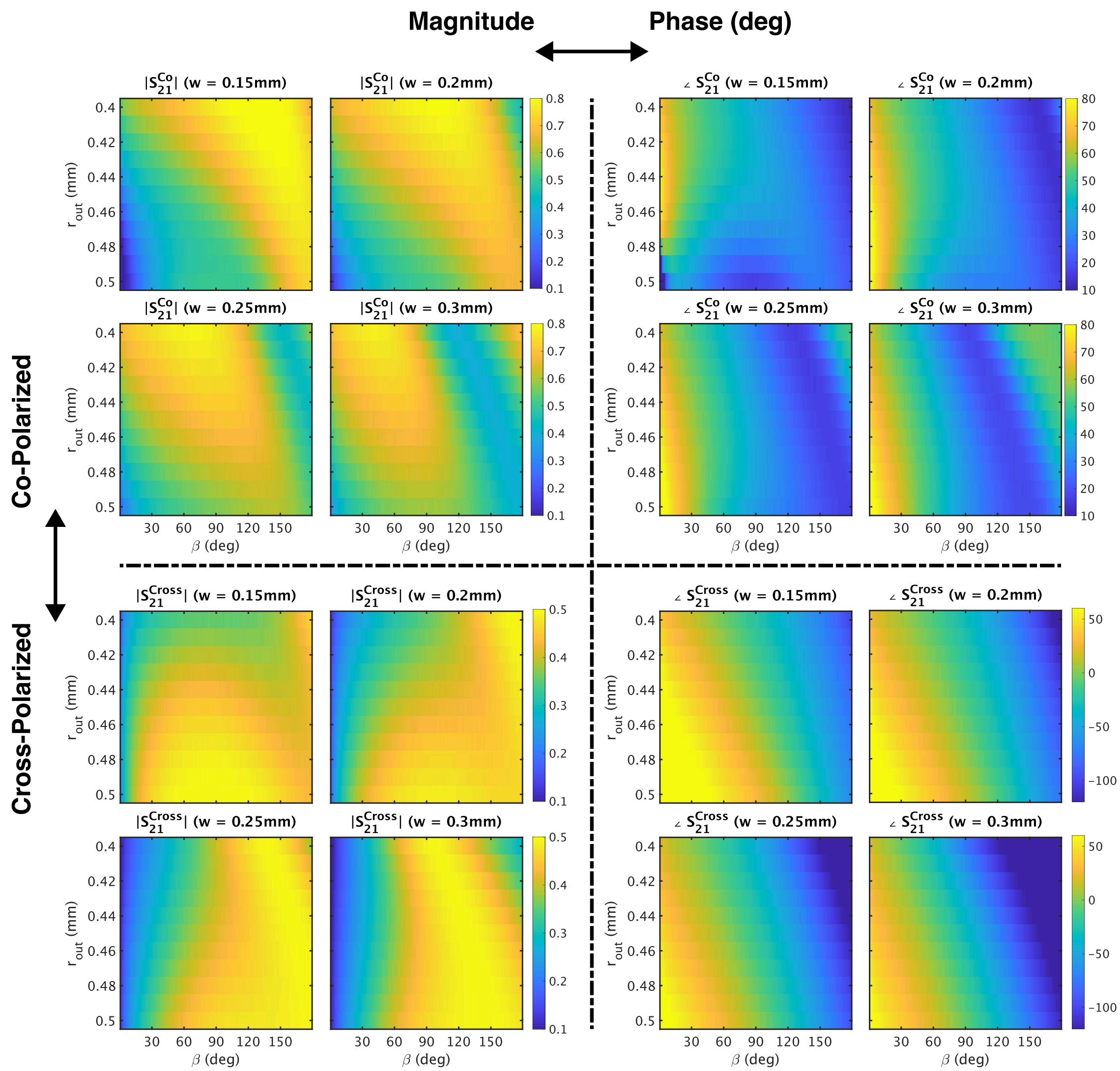

Figure S3: Simulated co- and cross-polarized transmission coefficients of C-shaped SRR geometries at 140 GHz, swept over outer radius r_{out} and split opening angle β for different strip widths w. Each geometry defines a physically realizable anisotropic response and a unique dictionary state.

Supplementary Note 4: Auxiliary Optimization Constraints/Penalties

The core metasurface optimization objective in this work is defined based on the expected link discovery error under a noise-driven confusion model. For each ground-truth direction θ_k, candidate directions with smaller Mahalanobis distance in the feature space are assigned higher confusion probabilities, and the resulting expected angular error $\mathcal{L}_k$ is averaged over the FoV to obtain the total core objective $\mathcal{L}$. This encourages polarization signatures to be both well separated and order preserving, such that residual confusions occur primarily between nearby directions. While minimizing $\mathcal{L}$ captures the essence of improving link discovery accuracy, optimizing this term alone is not sufficient for practical robustness. In particular, two additional issues must be handled in metasurface synthesis: feature unreliability near nulls, and heavy-tail failures from a small set of ambiguous directions. To explicitly address these issues, we introduce two auxiliary penalties in the optimization objective.

First, when either polarization component approaches the receiver noise floor, the measured polarization signatures become unreliable. Mathematically, if $|F_H(\theta)|$ or $|F_V(\theta)|$ contains deep nulls over the FoV, the extracted magnitude ratio ρ and phase difference $\Delta\phi$ become dominated by noise and hardware artifacts at these nulls, regardless of how well-separated the noiseless signatures may appear. Intuitively, link discovery fails when either polarization channel carries negligible energy, because the measured signature is no longer a stable representation of the underlying direction. Therefore, the optimized metasurface should avoid deep nulls in both polarization channels and maintain sufficient received power across the FoV. To enforce this requirement, we introduce a soft noise-floor penalty p_{noise} that discourages metasurface designs that yield deep nulls (below a certain threshold) in either polarization channels within the FoV:

$$p_{\text{noise}} = \frac{1}{K}\left[\sum_{k=1}^{K} \max\{0, T_H - M_H(\theta_k)\}^2 + \sum_{k=1}^{K} \max\{0, T_V - M_V(\theta_k)\}^2\right], \tag{S12}$$

where T_H and T_V are magnitude thresholds in dB scale, $M_H(\theta_k) = 20\log_{10}|F_H(\theta_k)|$, and $M_V(\theta_k) = 20\log_{10}|F_V(\theta_k)|$. As shown, both deeper null violations and more frequent violations would increase the penalty. While this term does not force a perfectly flat radiation pattern, it discourages designs that achieve "fake" signature separability by allowing one polarization channel to vanish at certain angles.

Second, the total expected error $\mathcal{L}$ may still hide a small number of directions with substantially larger errors. These ambiguity spots arise when a local cluster of signatures becomes difficult to distinguish, producing a heavy-tailed error distribution even if the average performance remains acceptable. To reduce such failures, we add a tail penalty p_{tail} that directly penalizes the most ambiguous directions. Let $\mathcal{L}^{(1)} \geq \mathcal{L}^{(2)} \geq \cdots \geq \mathcal{L}^{(K)}$ denote the sorted values of $\{\mathcal{L}_k\}_{k=1}^{K}$ in descending order, we define:

$$p_{\text{tail}} = \frac{1}{K_{\text{tail}}} \sum_{i=1}^{K_{\text{tail}}} \mathcal{L}^{(i)}. \tag{S13}$$

This term encourages more uniform link discovery performance across the FoV by explicitly suppressing the top K_{tail} largest errors.

Finally, the overall optimization objective used to evaluate each candidate metasurface layout is defined as:

$$\mathcal{J} = \mathcal{L} + \lambda_{\text{noise}} \cdot p_{\text{noise}} + \lambda_{\text{tail}} \cdot p_{\text{tail}}, \tag{S14}$$

where λ_{noise} and λ_{tail} are tunable hyperparameters that control the tradeoff among expected link discovery error, noise-floor robustness, and ambiguity-spot regularization. This objective is used as the fitness function in our genetic algorithm.

Supplementary Note 5: Details of the Genetic Algorithm

We use a genetic algorithm (GA) to search over the dictionary-constrained metasurface design space. Here, we provide the implementation details of this optimization. The purpose of the GA is to find a discrete metasurface layout that minimizes the objective $\mathcal{J}$, which jointly captures expected link discovery error, noise-floor robustness, and ambiguity-spot regularization.

We encode each candidate metasurface layout as an integer chromosome $\mathbf{x} = [x_1, x_2, \ldots, x_N]$ (i.e., an *individual*), where $x_n \in \{1, 2, \ldots, 15752\}$ is the dictionary index assigned to the n^{th} position of the 1D metasurface aperture. Each dictionary index uniquely specifies a physically realizable C-shaped SRR response, including its coupled co- and cross-polarized transmission coefficients. Given a chromosome $\mathbf{x}$, we retrieve the corresponding unit-cell responses from the dictionary, compute the anisotropic radiation patterns $F_H(\theta)$ and $F_V(\theta)$, construct the resulting polarization signature library $\{(\rho_k, \Delta\phi_k)\}_{k=1}^{K}$, and evaluate the fitness value $\mathcal{J}$. Lower values of $\mathcal{J}$ correspond to better individuals.

The initial *population* is generated randomly over the dictionary, but with a bias toward higher-transmission unit cells. Specifically, unit cells with larger combined transmission magnitude (i.e., $|S_{21}^{\text{Co}}| + |S_{21}^{\text{Cross}}|$) are sampled with higher probability during initialization. This bias prevents early populations from being dominated by highly lossy cells that largely suppress transmitted power, while still preserving diversity across the dictionary. In practice, this improves early convergence without constraining the GA to a small subset of unit cells. After initialization, the GA iteratively evolves the population through the following:

- **Selection:** Individuals with lower $\mathcal{J}$ are more likely to be selected as *parents*, biasing the evolution toward promising regions of the design space while preserving diversity through probabilistic selection.

- **Crossover:** Two parent individuals exchange subsets of their dictionary indices to form *children*, allowing "good substructures" to be recombined across candidates (i.e., groups of meta-elements that produce useful signature components).

- **Mutation:** Individuals not selected for crossover go through mutation, where a subset of *genes* (i.e., metasurface elements) are randomly reassigned to inject novelty, creating new substructures to be evaluated.

We also apply elitism at every *generation*. A small number of the best-performing individuals (i.e., *elites*) are copied unchanged into the next generation before crossover and mutation are applied to the rest of the population. This prevents stochastic operations from discarding the best layout found so far and makes the optimization trajectory more stable.

For the link discovery scheme proposed in the main manuscript, we optimize a 1D metasurface layout with $N = 50$ elements and subsequently tile it across rows to form a 2D aperture for enhanced azimuthal gains. The GA is run with a population size of 1500 individuals, including 15 elites per generation. We use a crossover factor of 0.6, meaning that 60% of the non-elite offspring are generated through crossover and the remaining non-elite offspring are generated through mutation. The optimization is terminated when either the maximum number of 5000 generations is reached or the best objective value has not improved for 500 consecutive generations. Fitness evaluations are independent across individuals and are therefore parallelized across CPU cores to reduce runtime.

After convergence, we select the individual with the lowest objective value as the optimized metasurface layout. The resulting layout used in the main manuscript is shown below in Fig. S4. Since the objective $\mathcal{J}$ is only a computationally efficient proxy for end-to-end link discovery performance, the final candidate is further evaluated through noise-injection simulations (e.g., via Monte Carlo trials) and, subsequently, over-the-air measurements. This final validation ensures that the optimized signature map remains robust under practical measurement noise and hardware non-idealities, rather than only performing well under the deterministic and ideal array-factor model used during GA iterations.

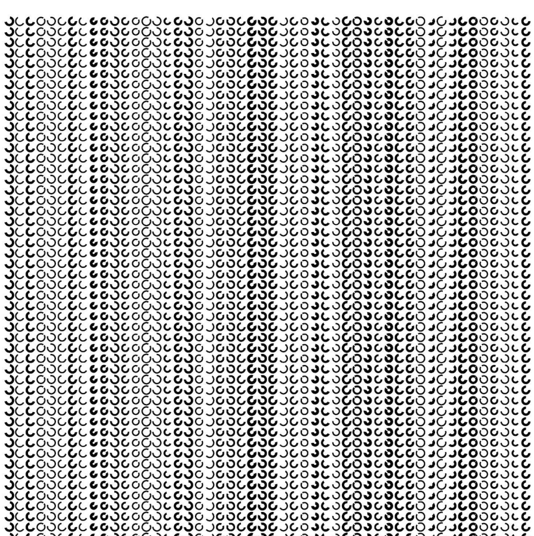

Figure S4: The exact optimized metasurface layout (50×50 elements) used for link discovery in the main manuscript.

Supplementary Note 6: Experiment Setup

Here, we provide a visual explanation of the measurement setup used for over-the-air validation of the proposed link discovery scheme. Fig. S5a provides an overview of the physical platform, where the transmitter, metasurface, and receiver are aligned at the same height. As such, the link-discovery problem in measurement is constrained to the 2D azimuthal plane. In addition to sweeping the azimuth angle, we also evaluate the impact of transmit-receive distance by moving the receiver along the propagation direction. Further, we evaluate the impact of receiver orientation by rotating the receiver around its roll axis. The detailed metasurface fabrication, signal generation, up/down-conversion, averaging, and offline feature extraction procedures are provided in the **Methods** section of the main manuscript.

At the transmit side, shown in Fig. S5b, a V-polarized D-band antenna illuminates the optimized anisotropic metasurface through a custom-fabricated dielectric lens. The power amplifier provides approximately 20 dB gain across the D-band. The collimating lens is used to combat the near-field spherical wavefront emitted by the transmitter and to approximate spatially uniform quasi-planar illumination across the metasurface aperture. The metasurface is fabricated through hot stamping following the optimized layout shown in Fig. S4. The transmit-side assembly is mounted on a motorized rotational stage whose rotation center is aligned with the center of the metasurface, allowing controlled azimuthal sweeps while maintaining the intended geometry.

At the receive side, shown in Fig. S5c, a dual-polarized D-band receiver captures the horizontal and vertical field components. The receiver consists of a dual-polarized antenna, an orthomode transducer (OMT), and two independent processing/down-conversion chains connected to two channels of the oscilloscope. This custom receiver module was built by Keysight and VDI to enable simultaneous complex measurements of the two polarization components. For investigation on receiver orientations, the receiver module is placed in a custom 3D-printed case mounted on a rotational stage, such that it rotates with respect to the phase center of the receiving horn. The receiver is also mounted on a translational stage for distance-dependent measurements. The measured H and V waveforms are recorded by the oscilloscope and processed offline to extract the complex polarization signatures used for link discovery.

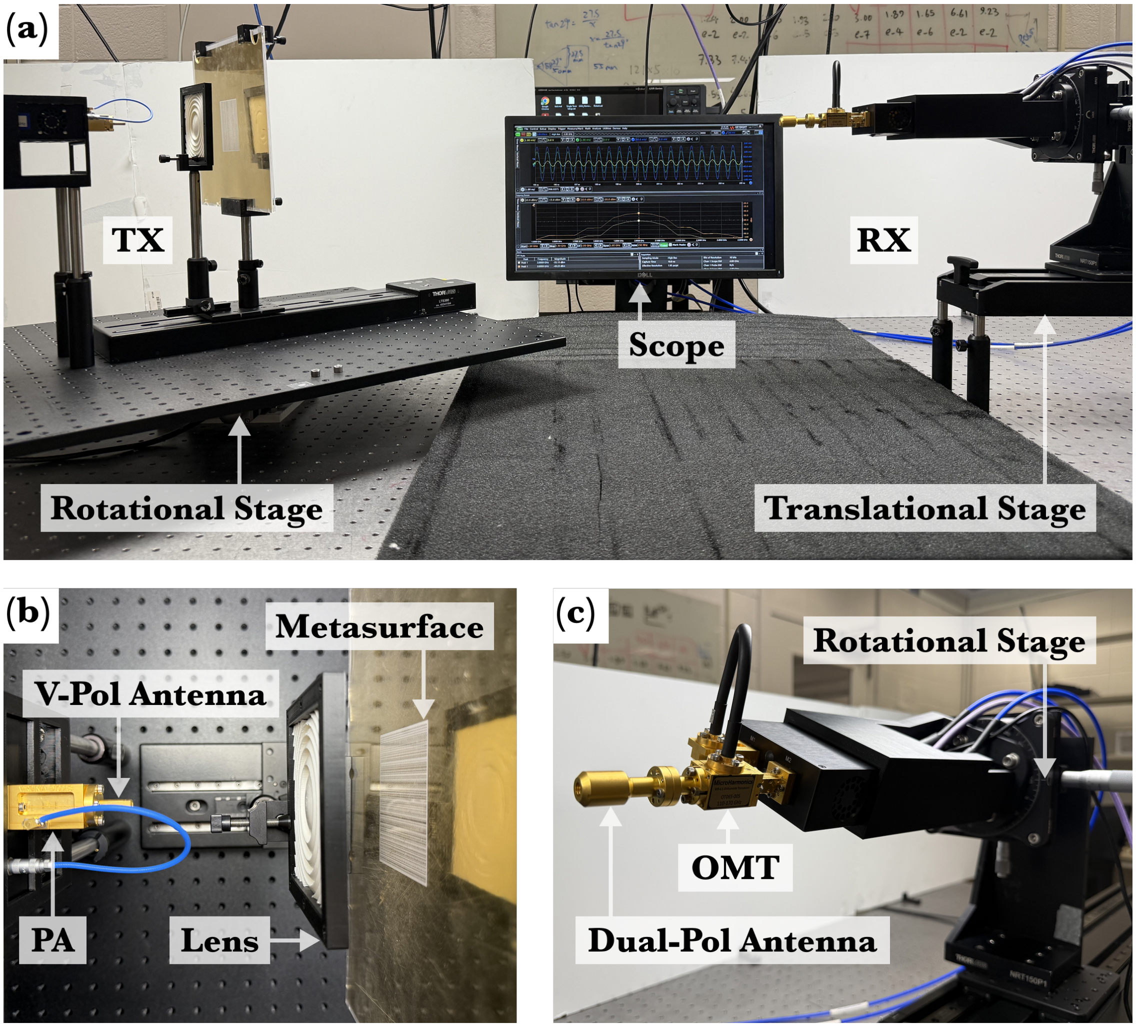

Figure S5: (a) Overview of the over-the-air setup, where the metasurface is illuminated by a V-polarized D-band transmitter and the polarization-resolved response is recorded by a dual-polarized receiver. The transmit side is mounted on a rotational stage for angular sweeps, and the receiver is mounted on a translational stage for distance-dependent measurements. (b) The transmit-side setup includes a power amplifier, a V-polarized antenna, a dielectric collimating lens, and a fabricated metasurface. (c) The receive-side setup includes a custom dual-polarized receiver module mounted on a rotational stage to investigate receiver orientation.

Supplementary Note 7: Impact of Surface Size

The main manuscript evaluates link-discovery performance using a 50×50 element metasurface, as shown in Fig. S4. Here, we expand the evaluation to the impact of metasurface aperture size (i.e., the number of surface elements). Since the polarization signatures $\{(\rho_k, \Delta\phi_k)\}_{k=1}^{K}$ depend on the coherent superposition of all anisotropic unit-cell responses, changing the aperture size does not simply scale the same design. Instead, increasing the aperture size exponentially expands the metasurface design space. Therefore, for each aperture size considered here, we independently re-optimize the metasurface layout using the same dictionary-constrained genetic algorithm described in Supplementary Note 5.

We design and fabricate metasurfaces with 40×40, 50×50, and 60×60 elements. Following the procedure from the main manuscript, we perform repeated over-the-air measurements and evaluate link discovery by using one measurement round as the reference library and the remaining rounds as tests. As shown in Fig. S6a, all three optimized surfaces achieve similar measured performance at a fixed transmit-receive distance of 80cm. The single-tone $\pm2^\circ$ accuracy remains around 93%, while concatenating signatures over three tones across a 1 GHz band increases the accuracy to $\sim$ 100% for all evaluated aperture sizes. This result shows that the proposed polarization-coded link discovery is not restricted to a single specific aperture size, as long as the metasurface is re-optimized for the chosen number of elements.

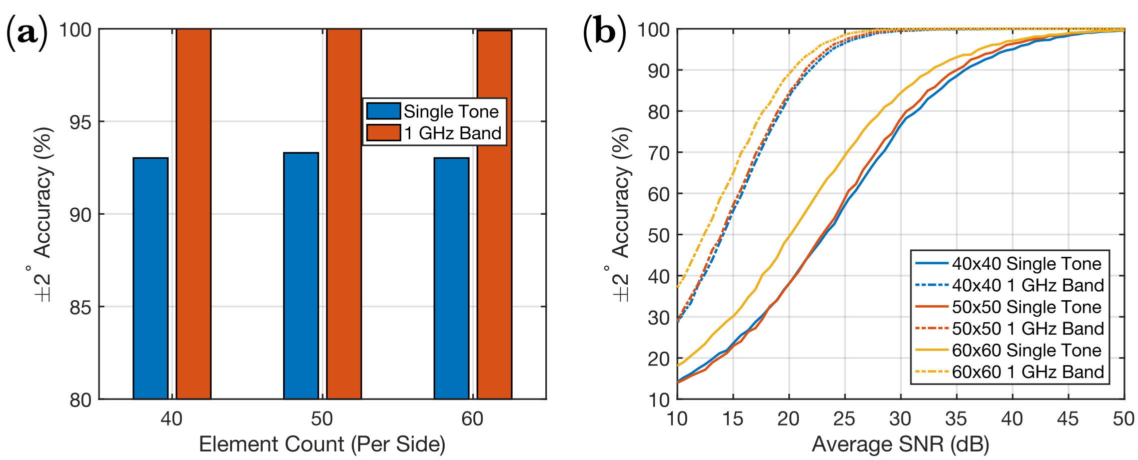

Figure S6: (a) Measured $\pm2^\circ$ accuracy for independently optimized metasurfaces with 40×40, 50×50, and 60×60 elements, evaluated using repeated over-the-air measurements. (b) $\pm2^\circ$ accuracy under controlled noise injection in the measured radiation patterns and Monte Carlo trials.

We further evaluate the robustness of these measured signatures under controlled noise injection. Specifically, we use the measured radiation patterns as the reference signature maps and inject controlled complex noise at different average SNR levels before performing link discovery. Fig. S6b shows the resulting $\pm 2^\circ$ accuracy as a function of SNR (averaged across the FoV). We observe that the 1 GHz-band aggregation significantly improves robustness to noise compared with single-tone operation across all three aperture sizes, consistent with the main manuscript. At lower SNRs, the larger 60×60 metasurface shows a clear robustness advantage, while the 40×40 and 50×50 designs perform similarly. This is consistent with the intuition that a larger aperture expands the design space, increases array-factor gain, and enables faster-varying polarization signatures across angle. However, the trend is not purely deterministic because each aperture size is independently optimized over a large discrete and non-convex space. Thus, additional elements increase the potential for more robust link discovery, but the final performance still depends on the specific GA-optimized signature map obtained for that surface size.

Overall, these results confirm that surface size is an important design parameter, but the proposed framework remains robust across practical aperture choices. Increasing the number of elements provides more spatial degrees of freedom, while the final performance depends on how effectively the optimization converts those degrees of freedom into noise-robust and order-preserving polarization signatures.

Supplementary Note 8: Near-Field Considerations

The polarization signature model in the main manuscript is most naturally interpreted in the far field, where the angular radiation pattern is approximately distance-invariant. Under this condition, a signature library measured at one distance can be reused at other distances, because common propagation loss is canceled in the V/H magnitude ratio ρ and does not affect the $V - H$ phase difference $\Delta\phi$. However, in the radiative near field of an electrically large metasurface, the received polarization signature can vary with both angle and distance. This is because the receiver observes a finite-distance coherent superposition of fields radiated by many anisotropic elements, rather than a fully formed far-field angular pattern.

Fig. S7a illustrates this effect by plotting the measured magnitude-ratio feature ρ across the FoV at different transmit-receive distances. While the overall structure of the signature remains similar, small distance-dependent variations are visible. These variations can perturb the nearest-neighbor matching process if the same reference library is used for all distances. Therefore, in the main measurements, we calibrate the signature library at the corresponding measurement distance before evaluating link discovery accuracy.

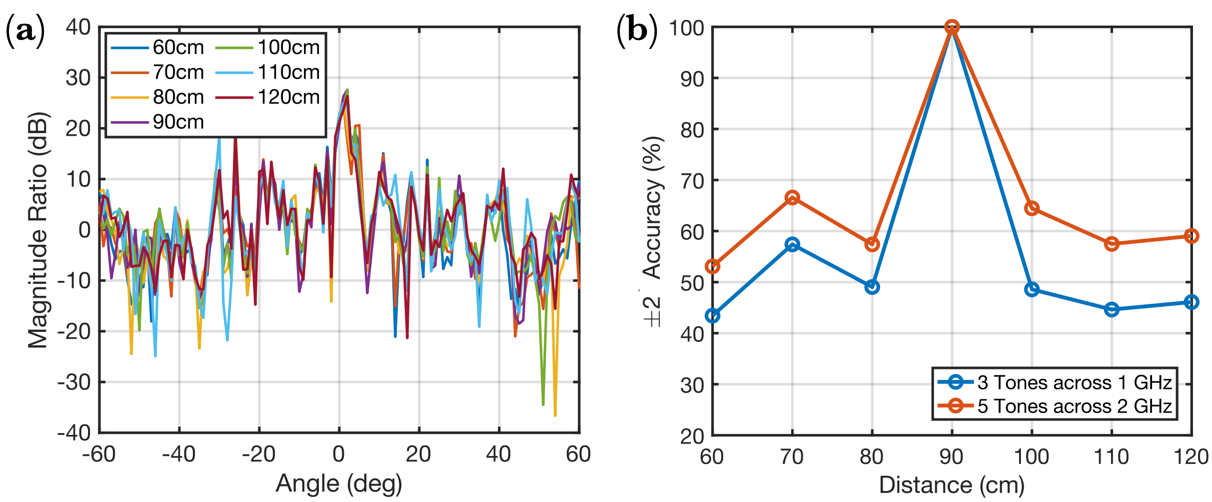

Figure S7: (a) Measured magnitude-ratio feature ρ across angles at different transmit-receive distances, showing small but visible distance-dependent signature variations. (b) Link-discovery accuracy when a single reference library measured at 90 cm is reused for all distances without calibration.

To show the impact of ignoring this distance dependence, Fig. S7b evaluates link discovery when a single reference library measured at 90 cm is reused for all other distances. In this case, the accuracy is highest at 90 cm, where the reference and test distances match, but degrades at other distances due to near-field signature mismatch. Fig. S7b shows that multi-tone measurements can mitigate this mismatch. When the feature vector is expanded from 3 tones across a 1 GHz band to 5 tones across a 2 GHz band, link-discovery accuracy improves at all mismatched distances. This improvement suggests that frequency diversity helps separate the intended angle-dependent polarization coding from distance-dependent near-field artifacts. Therefore, while distance-specific calibration remains the most reliable approach in the current prototype, wider-band or denser multi-tone operation can reduce sensitivity to near-field distance mismatch.

Finally, we note that distance-dependent near-field signatures are not necessarily undesirable. In principle, if the signature varies jointly with angle and distance in a stable manner, the same polarization-coded metasurface could support single-shot two-dimensional localization over both azimuth angle and range. We leave this extension to future studies.

Supplementary Note 9: Measurement Noise

In the main manuscript and Supplementary Note 1, we model the feature noise from independent and complex Gaussian noise in the H- and V-polarized channels. Here, we experimentally characterize this noise in our over-the-air setup and verify that the observed feature fluctuations are consistent with the model. We also demonstrate that our measurements operate in a high-SNR regime.

We first fix the transmitter, metasurface, and receiver geometry and repeatedly measure the same polarization signature over a 10-minute interval. Fig. S8a-b show the measured magnitude ratio ρ and phase difference $\Delta\phi$ over time. We observe slow oscillations and random jitters in both dimensions, caused by common high-frequency experimental artifacts including asynchronous LOs on transmitting and receiving sides, phase drifts between independent H and V RF chains, and thermal perturbations. The observed standard deviations are $\sigma_\rho = 0.31$ dB and $\sigma_{\Delta\phi} = 1.93°$. We note that this corresponds to a feature noise ratio of 9.2 dB/rad, which is close to the theoretical scaling factor $20/\ln 10 \approx 8.7$ derived in Eq.(S7) from Supplementary Note 1.

Further, we measure this feature noise across the entire FoV, over the 10 rounds of measurements used for link-discovery evaluations. Here, we estimate that the average received SNR across the FoV is around 40 dB in our setup. This SNR level is consistent with the high-accuracy operating region observed in the noise-injection experiments in the main manuscript, where link discovery remains robust. Finally, Fig. S8c-d show that the feature noise is not uniform across angles. Both ρ and $\Delta\phi$ noise standard deviations vary over the FoV, with larger fluctuations appearing near angles where the measured polarization channels are weaker and more sensitive to small perturbations. The two feature-noise curves also vary together, consistent with the derivation in Supplementary Note 1, where both $\sigma^2_{\rho,k}$ and $\sigma^2_{\Delta\phi,k}$ depend on the same local H- and V-polarized field magnitudes. This angle-dependent noise behavior motivates the use of the Mahalanobis distance (rather than a fixed Euclidean distance) when computing confusion probabilities during metasurface optimization.

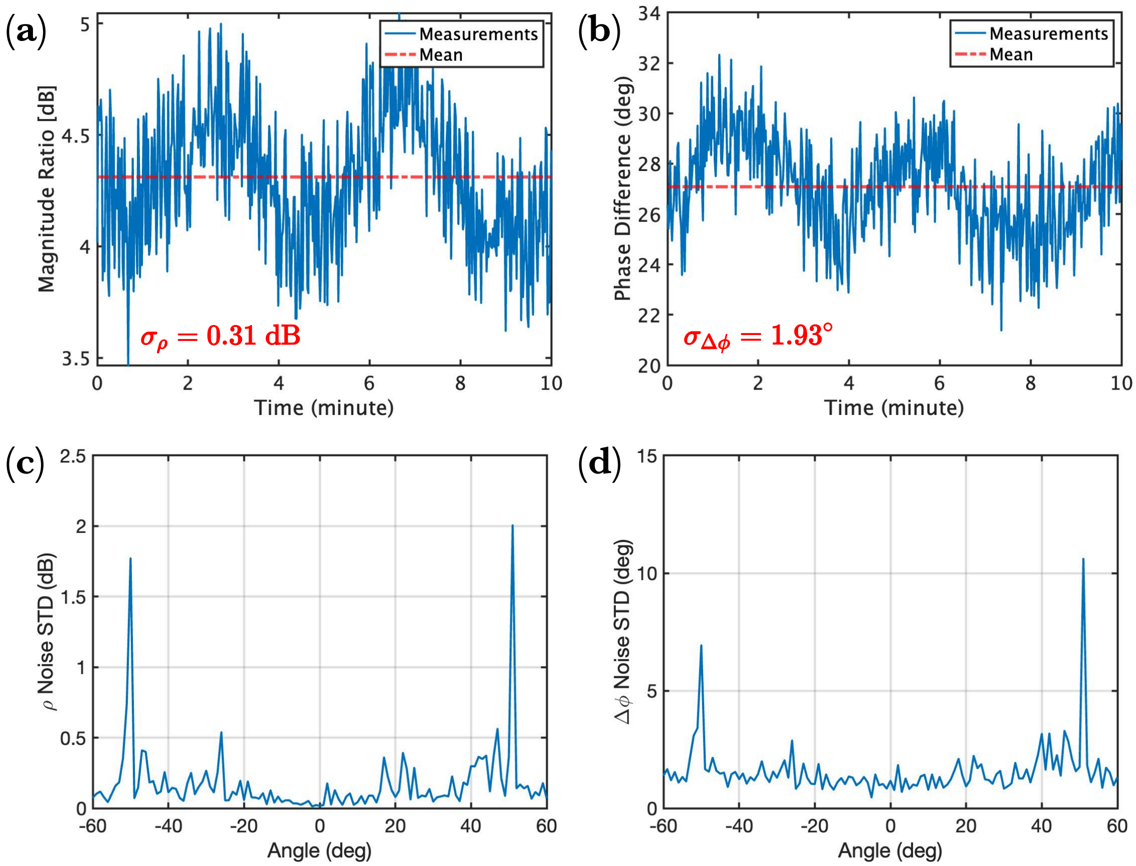

Figure S8: (a-b) Measured magnitude ratio ρ and phase difference $\Delta\phi$ over a 10-minute interval under a fixed geometry, showing standard deviations of 0.31 dB and 1.93°, respectively. (c-d) Angle-dependent feature noise standard deviations of ρ and $\Delta\phi$, showing that feature-space uncertainty can vary with direction.

Supplementary Note 10: Link Discovery under Receiver Rotations

So far, link discovery has been evaluated with a fixed receiver orientation, with its polarization basis aligned to the reference H/V axes (at the transmitter). In practice, however, the receiver may experience roll rotations that mix the two measured polarization components. Here, we describe how such receiver rotations can be modeled and compensated, and we experimentally evaluate the robustness of link discovery under inaccurate estimations of receiver orientation. All results in this section use multi-tone signatures from 5 tones across a 2 GHz band.

First, at a given frequency f, we write the recorded electric field library under the reference receiver orientation as $\tilde{\mathbf{E}}(\theta, f) = [\tilde{E}_H(\theta, f), \tilde{E}_V(\theta, f)]^\mathsf{T}$. In practice, raw measurements of $\tilde{\mathbf{E}}$ are captured under complex responses of the two receiver polarization chains. While this artifact is absorbed in the fingerprinting process for previous link discovery evaluations, it needs to be compensated for rotation-related operations. Specifically, the calibrated (nominal) over-the-air electric-field can be retrieved with

$$\mathbf{E}(\theta, f) = \begin{bmatrix} E_H(\theta, f) \\ E_V(\theta, f) \end{bmatrix} = \begin{bmatrix} g_H(f)^{-1} & 0 \\ 0 & g_V(f)^{-1} \end{bmatrix} \tilde{\mathbf{E}}(\theta, f), \tag{S15}$$

where $g_H(f)$ and $g_V(f)$ capture the frequency-dependent complex responses of the two receiver chains. In our code implementation, $g_V(f)$ is taken as the reference and set to 1, while $g_H(f)$ is calibrated at each measured tone. We note that $g_H(f)$ is obtained through a one-time calibration (using known rotations) with a complex grid search over relative amplitude and phase offsets, selecting the value that minimizes the mismatch between the predicted and the measured rotated library across the FoV. This calibration accounts for the imbalanced hardware responses of the dual-polarized antenna, OMT, and down-conversion chains before applying the polarization-basis rotation.

With the calibrated nominal electric fields $\mathbf{E}$, we can rotate it to fit any known receiver rotation angle γ (e.g., estimated through inertial sensors). Under ideal basis rotation, the raw measured library corresponding to a receiver rotated by γ can be predicted as:

$$\hat{\mathbf{E}}(\theta, f \,|\, \gamma) = \begin{bmatrix} g_H(f) & 0 \\ 0 & g_V(f) \end{bmatrix} \mathbf{R}(\gamma)\, \mathbf{E}(\theta, f), \text{ where } \mathbf{R}(\gamma) = \begin{bmatrix} \cos\gamma & -\sin\gamma \\ \sin\gamma & \cos\gamma \end{bmatrix} \tag{S16}$$

These predicted rotated fields $\hat{\mathbf{E}}$ and test measurements $\tilde{\mathbf{E}}$ are then converted into multi-tone signatures and matched using the same nearest-neighbor procedure for link discovery.

Fig. S9a evaluates this procedure experimentally using a reference library measured under no receiver rotation. For each receiver rotation angle, the baseline library is transformed to the corresponding orientation using Eq.(S15) and Eq.(S16) before signature matching. Link discovery remains accurate over a wide range of rotations, but gradually degrades at larger roll angles. This degradation is expected because practical receiver rotations are not a perfect polarization-basis rotation: the mechanical alignment can introduce small non-idealities that become more visible at larger rotations. It is worth noting that the important quantity here is the relative rotation between the library and the test measurement. For example, if a library is measured at a large receiver roll angle such as 70°, then testing at a nearby orientation such as 90° can still perform well because the relative rotation is small. In practical systems, robustness can therefore be improved by recording a small number of reference libraries at representative receiver orientations, such as 0° and 90°, and matching each test measurement to the closest reference basis.

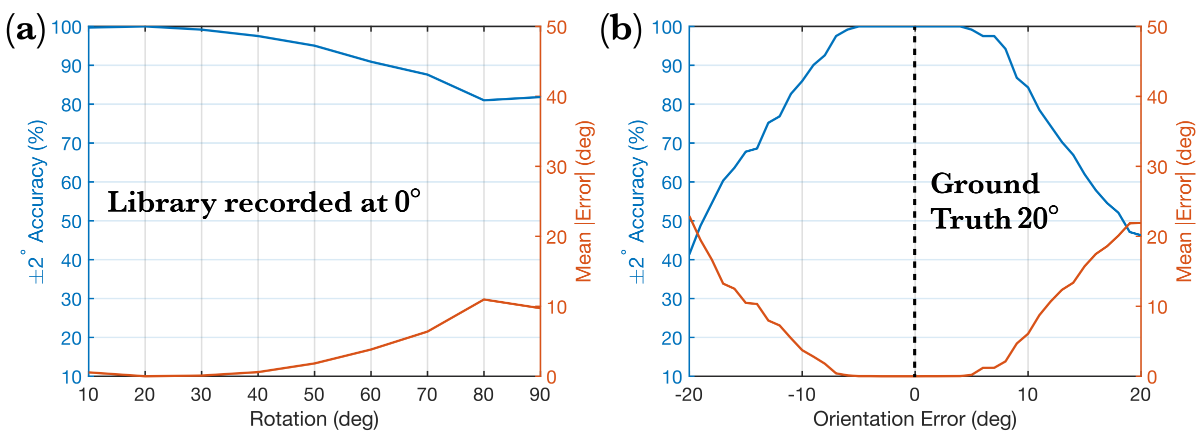

Figure S9: (a) Link-discovery performance under different receiver rotation angles using a reference library measured at 0°. (b) Robustness to estimation errors of receiver orientation, under a ground-truth orientation of 20°. High link-discovery accuracy is preserved under small orientation-estimation errors.

Finally, Fig. S9b evaluates the sensitivity to orientation-estimation errors under a fixed 20° ground truth receiver orientation. The result shows that link-discovery accuracy remains high when the orientation estimate is within ±7° degrees of the true value, indicating that link discovery does not rely on perfectly precise receiver-orientation knowledge.

Supplementary Note 11: Link Discovery under Multipath Reflections

So far, the proposed polarization-coded link discovery has been evaluated strictly under line-of-sight (LOS) conditions. Here, we study how practical multipath scenarios can impact link discovery performance. As illustrated in Fig. S10, we consider a planar reflector placed parallel to the LOS direction, creating an additional non-line-of-sight (NLOS) path that coherently combines with the LOS signal at the receiver.

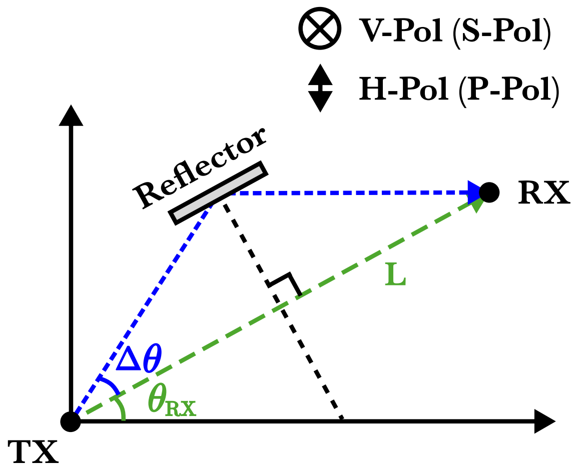

Figure S10: A planar and ideal reflector (parallel to LOS path) introduces a specular NLOS path that coherently combines with the LOS signal at the receiver. For simplicity in the Fresnel reflection model, the transmitter and receiver are positioned such that V-polarization corresponds to S-polarization and H-polarization corresponds to P-polarization of the reflection plane.

Under this geometry, the vertical polarization lies perpendicular to the plane of incidence and therefore corresponds to the S-polarized component, while the horizontal polarization lies in the plane of incidence and corresponds to the P-polarized component. As a result, the two reflected polarization components experience different Fresnel coefficients. For a dielectric reflector, these coefficients are given by:

$$\Gamma_s = \frac{n_1 \cos\theta_i - n_2 \cos\theta_t}{n_1 \cos\theta_i + n_2 \cos\theta_t}, \qquad \Gamma_p = \frac{n_2 \cos\theta_i - n_1 \cos\theta_t}{n_2 \cos\theta_i + n_1 \cos\theta_t}, \tag{S17}$$

where $n_1 = 1$ is the refractive index of air, $n_2 = \sqrt{\epsilon_r \mu_r} \approx \sqrt{\epsilon_r}$ is the refractive index of the reflector material, $\theta_i = 90° - |\Delta\theta|$ is the incidence angle, and $\theta_t = \arcsin\left(\frac{n_1}{n_2}\sin\theta_i\right)$ is the transmission angle determined by Snell's law.

We then model the measured polarization components as the coherent sum of the LOS field and a reflected NLOS field:

$$\begin{cases} \tilde{E}_V = E_V(\theta_{\mathrm{RX}}) + \alpha_l \, \Gamma_s(\Delta\theta) \, E_V(\theta_{\mathrm{RX}} + \Delta\theta) \, e^{-jk\Delta L} \\ \tilde{E}_H = E_H(\theta_{\mathrm{RX}}) + \alpha_l \, \Gamma_p(\Delta\theta) \, E_H(\theta_{\mathrm{RX}} + \Delta\theta) \, e^{-jk\Delta L} \end{cases}, \tag{S18}$$

where ΔL is the excess path length of the reflected path relative to the LOS path (a function of $\Delta\theta$), k is the wavenumber, and α_l is the additional attenuation factor in the NLOS path (e.g., from surface roughness, scattering, finite reflector size, edge diffraction, reflector rotation, layered material, and other non-idealities). The Fresnel terms capture the polarization-dependent reflection response, while $e^{-jk\Delta L}$ captures the coherent phase shift from the excess path length. After computing the perturbed fields $\tilde{E}_V$ and $\tilde{E}_H$, we can extract the corresponding polarization signatures ρ and $\Delta\phi$ and evaluate link discovery against the LOS-calibrated reference library.

Fig. S11a shows the Fresnel reflection loss as a function of the angular separation $|\Delta\theta|$ between the LOS and reflected directions. Here, to systematically evaluate the impact of multipath reflections, we first compute the Fresnel loss under different relative permittivities (ϵ_r), defined as:

$$L_{\text{refl}}(\Delta\theta) = 10\log_{10}\left(\frac{|\Gamma_s(\Delta\theta)|^2 + |\Gamma_p(\Delta\theta)|^2}{2}\right). \tag{S19}$$

In our geometry, smaller $|\Delta\theta|$ corresponds to more grazing incidence, which leads to stronger specular reflection and therefore smaller reflection loss. As $|\Delta\theta|$ increases, the Fresnel reflection magnitude decreases, and the NLOS path becomes weaker. As expected, reflectors with higher permittivities produce stronger reflections.

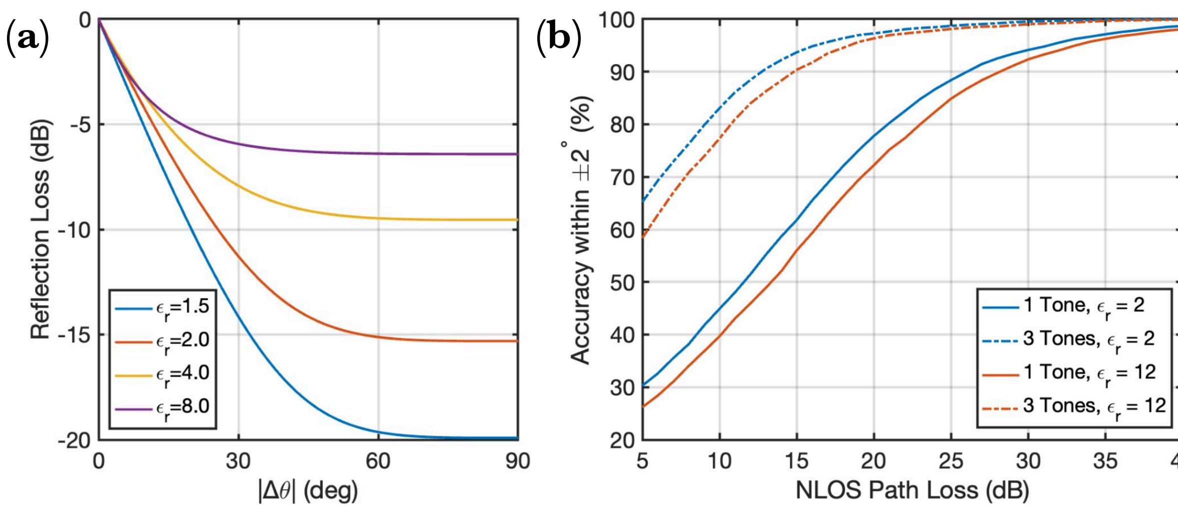

Figure S11: (a) Fresnel reflection loss versus reflected-path angular offset $|\Delta\theta|$ for different dielectric constants. Smaller $|\Delta\theta|$ corresponds to more grazing incidence and stronger reflection. (b) Simulated $\pm 2^\circ$ link-discovery accuracy under a single reflected path, evaluated as a function of additional NLOS-to-LOS path loss (α_l).

We then run deterministic simulations using the measured LOS radiation patterns as the reference library. Specifically, we enumerate all feasible pairs of the true angle θ_{RX} and reflected-path offset $\Delta\theta$ such that the NLOS direction remains inside the measured FoV. For each feasible configuration, the observed electric field is calculated as the coherent sum of the LOS component and the specular NLOS component following Eq.(S18). Fig. S11b shows the resulting $\pm 2^\circ$ accuracy as a function of additional NLOS path loss (α_l). As expected, link discovery is more difficult when the reflected path is strong, because the received H and V components become distorted by the reflected signal. Accuracy improves as the NLOS path loss increases, approaching the LOS performance when the reflected component becomes sufficiently weak. The figure also shows that multi-tone operation substantially improves robustness compared with single-tone operation, as frequency diversity across tones provides a richer signature for matching. Finally, higher-permittivity reflectors produce stronger reflections and therefore slightly lower accuracy under the same additional NLOS path loss, consistent with the reflection-loss trend in Fig. S11a. We note that typical dielectric constants of everyday indoor materials generally fall within a moderate range, with many plastics, wood, drywall, glass, and concrete-like materials lying approximately between $\epsilon_r = 2$ and $\epsilon_r = 12$. Therefore, we use this range to represent common dielectric reflectors in this study.